Tracing the 10^7 K warm–hot intergalactic medium with UV absorption lines

A. Fresco, C. Péroux, A. Merloni, A. Hamanowicz, R. Szakacs

To cite this version:

A. Fresco, C. Péroux, A. Merloni, A. Hamanowicz, R. Szakacs. Tracing the 10^7 K warm–hot intergalactic medium with UV absorption lines. Monthly Notices of the Royal Astronomical Society, 2020, 499 (4), pp.5230-5240. 10.1093/mnras/staa2971 . hal-02966414

HAL Id: hal-02966414
https://hal.science/hal-02966414v1

Submitted on 25 May 2024

HAL is a multi-disciplinary open access archive for the deposit and dissemination of scientific research documents, whether they are published or not. The documents may come from teaching and research institutions in France or abroad, or from public or private research centers.

L'archive ouverte pluridisciplinaire **HAL**, est destinée au dépôt et à la diffusion de documents scientifiques de niveau recherche, publiés ou non, émanant des établissements d'enseignement et de recherche français ou étrangers, des laboratoires publics ou privés.

Monthly Notices
of the
ROYAL ASTRONOMICAL SOCIETY

MNRAS **499,** 5230–5240 (2020)
Advance Access publication 2020 September 26

doi:10.1093/mnras/staa2971

Tracing the 10^7 K warm–hot intergalactic medium with UV absorption lines

A. Y. Fresco,[1★] C. Péroux,[2,3] A. Merloni,[1] A. Hamanowicz[2] and R. Szakacs[2]

[1] *Max-Planck-Institut für Extraterrestrische Physik (MPE), Giessenbachstrasse 1, D-85748 Garching, Germany*
[2] *European Southern Observatory, Karl-Schwarzschildstrasse 2, D-85748 Garching bei München, Germany*
[3] *Aix Marseille Université, CNRS, LAM (Laboratoire d'Astrophysique de Marseille) UMR 7326, F-13388 Marseille, France*

Accepted 2020 September 17. Received 2020 September 17; in original form 2020 June 24

ABSTRACT

Today, the majority of the cosmic baryons in the Universe are not observed directly, leading to an issue of 'missing baryons' at low redshift. Cosmological hydrodynamical simulations have indicated that a significant portion of them will be converted into the so-called warm–hot intergalactic medium (WHIM), with gas temperature ranging between 10^5 and 10^7 K. While the cooler phase of this gas has been observed using O VI and Ne VIII absorbers at ultraviolet (UV) wavelengths, the hotter fraction detection relies mostly on observations of O VII and O VIII at X-ray wavelengths. Here, we target the forbidden line of [Fe XXI] λ 1354 Å which traces 10^7 K gas at UV wavelengths, using more than 100 high-spectral resolution ($R \sim 49\,000$) and high signal to noise VLT/UVES quasar spectra, corresponding to over 600 h of VLT time observations. A stack of these at the position of known Ly α absorbers lead to a 5σ limit of $\log[N([\mathrm{Fe\,XXI}])] < 17.4$ ($\mathrm{EW_{rest}} < 22$ mÅ), three orders of magnitude higher than the expected column density of the WHIM $\log[N([\mathrm{Fe\,XXI}])] < 14.5$. This work proposes an alternative to X-ray detected 10^7 K WHIM tracers, by targeting faint lines at UV wavelengths from the ground benefiting from higher instrumental throughput, enhanced spectral resolution, longer exposure times, and increased number of targets. The number of quasar spectra required to reach this theoretical column density with future facilities including 4MOST, ELT/HIRES, MSE, and the Spectroscopic Telescope appears challenging at present. Probing the missing baryons is essential to constrain the accretion and feedback processes that are fundamental to galaxy formation.

Key words: techniques: spectroscopic – Galaxy: evolution – Galaxy: formation – intergalactic medium – quasars: absorption lines – large-scale structure of Universe.

1 INTRODUCTION

The standard cosmological model predicts that the vast majority of the matter is in the form of dark energy and dark matter. Only the remaining 4 per cent is in the form of baryons, the 'normal matter' that makes stars and galaxies. The total baryon density of the Universe, $\Omega_{\mathrm{baryons}} = 0.0455$, is well constrained from measurements of cosmic microwave background (CMB) anisotropies (Aghanim et al. 2016), light element abundances coupled with big bang nucleosynthesis (Cooke & Fumagalli 2018) and, in the near future, from observations of dispersion measures of fast radio bursts (FRBs) (e.g. Macquart et al. 2020; Qiang & Wei 2020). We note that results from these different experiments involving vastly different physical processes and observation techniques agree remarkably well. However, 30–50 per cent of the baryonic matter is currently not observed directly (Persic & Salucci 1992; Nicastro et al. 2018; Peroux & Howk 2020). The latest baryon census shows that galaxies, groups, and clusters together comprise only ∼ 10 per cent of the expected baryon density (Salucci & Persic 1999; Bregman 2007; Shull, Smith & Danforth 2012; Nicastro et al. 2018; de Graaff et al. 2019). Recently, a fraction of these cooler baryons were found on the scales of the galaxy haloes, including in the circumgalactic medium (CGM) (Werk et al. 2013; Tumlinson, Peeples & Werk 2017). This still leaves a deficit of observed baryons relative to the predicted baryon density referred to as the 'missing baryons problem' (Bregman 2007; Shull et al. 2012).

At the turn of the century, cosmological hydrodynamical simulations of the large-scale structure have postulated on the phase and location of these missing baryons. At high redshift, the models indicate that the majority of the baryons are in the low-density ionized gas of the intergalactic medium (IGM). This phase is observationally traced by the Ly α forest that only provides direct constraints on the neutral fraction of a gas that is mostly ionized (Kim & Kim 2013). Therefore, baryons in IGM, although dominant at early epochs, remain challenging to observe. At lower redshifts, simulations of the matter distribution indicate that the baryons are related to a shock-heated phase of the gas with temperature range of $10^5\ \mathrm{K} < T < 10^7$ K, swiftly called warm–hot intergalactic medium (WHIM) (Cen & Ostriker 1999; Davé et al. 2001). According to these cosmological simulations, at $z = 0$, the WHIM is the dominant baryon contributor and is located mostly in filaments and knots along the cosmic web, in which groups and clusters reside (Martizzi

---

★ E-mail: yrufresquito@gmail.com

© 2020 The Author(s)
Published by Oxford University Press on behalf of the Royal Astronomical Society

Downloaded from https://academic.oup.com/mnras/article/499/4/5230/5912396 by guest on 25 May 2024

et al. 2019). A different approach using *Enzo* grid-code simulations challenges the postulate that a significant amount of WHIM has been shock-heated to 10^7 K. For example, Shull et al. (2012) find a small 'hot plume' at $T > 10^7$ K in the (T, b) phase diagram. Observational baryon-censuses also find that the Ly α forest contains ∼30 per cent of the baryons, with similar amounts in gas at $T = 10^{5-6}$ K probed by O VI and broad Ly α absorbers (BLAs). Speculation is that the remainder ('missing baryons') resides at higher temperatures ($T > 10^6$ K) that are not traced by O VI and BLAs.

Due to its diffuse nature, direct detection of the WHIM in emission poses a great observational challenge (Bertone, Schaye & Dolag 2008; Frank et al. 2010; Augustin et al. 2019; Wijers, Schaye & Oppenheimer 2020). To remedy this limitation, absorption lines detected against bright background objects offer the most compelling way to study the temperature, ionization state, and column density of the gas. In these absorbers, the minimum gas density detected is set by the brightness of the background source and thus the detection efficiency is independent of redshift and the foreground object's brightness.

Oxygen is one of the most useful tracers of the WHIM because of its high abundance and because O VI, O VII, and O VIII excitation states span nearly the entire 10^5–10^7 K temperature range. The doublet of C IV and Ly α contribute at the low end as well, while Ne VIII (at 770 and 780 Å) is associated with collisionally ionized gas at $T \approx 5 \times 10^5$ K (Narayanan et al. 2011). The O VI doublet is observable in ultraviolet (UV) with lines at 1032 and 1038 Å, which also makes them easy to identify (Howk et al. 2009). Unfortunately, the interpretation of O VI is complex. One issue is that O VI absorption turns out to be relatively easy to produce either from photoionization or collisional ionization (CIE). In CIE, the maximum fraction of Oxygen which is in O VI is only ∼20 per cent, so the ionization correction are likely considerable (Werk et al. 2014; Prochaska et al. 2017). Additionally, we need to specify a metallicity in order to convert from O VI into a baryon mass, which is usually unknown. The WHIM can be traced by Ly α absorption as well. These Ly α lines look different from the narrow lines typical of the photoionized gas, since they are also appreciably thermally broadened. These are the BLAs, and overlap with the O VI-traced WHIM (Pachat et al. 2016).

Hotter collisionally ionized gas emits soft X-rays, but the emissivity is proportional to the square of the gas density, which again limits the effectiveness of emission as a probe of low-density gas. X-ray analysis traces metal emission lines (for the CGM, primarily O VII and O VIII, but also iron lines). Owing to the lack of telescopes with adequate sensitivity in the X-ray wavelengths, the hot phase of the CGM traced by O VII and O VIII is as yet not well studied (Li 2020). These lines, which correspond to a series of soft X-ray features around 0.6–0.8 keV, are commonly detected at redshift zero, corresponding to the hot halo around the Milky Way (Gupta et al. 2012) (but see also Wang & Yao 2012). At moderate redshifts, they are also accessible with the grating spectrographs on *XMM–Newton* (Arcodia et al. 2018) and *Chandra* (sensitive down about to 0.35 and 0.2 keV, respectively). Unfortunately, current X-ray gratings have poor spectral resolution (700–800 km s^{-1}), and effective areas of tens of cm^2 (compared to 1000–3000 cm^2 for *HST-COS* in the UV), so they have limited sensitivity to the WHIM (DeRoo et al. 2020). The detection of two X-ray absorbers towards 1ES 1553+113 by Nicastro et al. (2018) (but see Johnson et al. 2019, for cautionary notes) is the latest indication that the missing baryons are indeed in a diffuse WHIM phase, although it remains unclear which fraction of the missing baryons are traced by X-ray absorbers. Overall, there are only a few X-ray observed WHIM absorbers (Bonamente et al. 2016; Mathur et al. 2017; Nicastro et al. 2018; Johnson et al. 2019; Nevalainen et al. 2019). The next generation X-ray observatories such as *Athena* (Barcons et al. 2011) and its high spectral resolution micro-calorimeter with about an order of magnitude higher effective area than *XMM–Newton* and *Chandra*, will make significant progress in the next decade (Barret et al. 2020). Until then, it is extremely important to study the warm-hot gas, using the existing UV and X-ray facilities.

Different methods have been proposed to detect the hot, highly ionized WHIM gas: detection in galaxy groups with Sunyaev–Zeldovich effect (Hill et al. 2016; de Graaff et al. 2019; Lim et al. 2020; Tanimura et al. 2020) using autocorrelation function measurements (Galeazzi et al. 2010), with absorption lines in quasar sightline (Kovács et al. 2019) and using CMB as a backlight (Ho, Dedeo & Spergel 2009). Given the challenges of X-ray data, observations at longer wavelengths (UV and optical) benefit from higher instrumental throughout, enhanced spectral resolution. By reverting to ground-based facilities, longer exposure times and larger number of targets become possible. Nevertheless, the UV lines have so far mostly been used to detect absorbing gas with temperature range 10^5 K $< T < 10^6$ K from either O VI (Tripp, Savage & Jenkins 2000; Danforth & Shull 2005; Danforth & Shull 2008; Tripp et al. 2008; Savage et al. 2014; Werk et al. 2014; Danforth et al. 2016; Sanchez, Morisset & Delgado-Inglada et al. 2016) or BLAs (Lehner et al. 2007; Danforth, Stocke & Shull 2010). Recently, Zastrocky et al. (2018) have constrained the Milky Way's hot ($T = 2 \times 10^6$ K) coronal gas using the forbidden 5302 Å transition of Fe XIV. Only recently, some highly ionized iron UV lines detected in emission have been used as diagnostics of gas at temperatures of $T = 10^7$ K. Out of several forbidden lines in the UV that could trace this gas temperature range, and from various species of highly ionized iron, the emission of [Fe XXI] is the brightest (Anderson & Sunyaev 2016). Anderson & Sunyaev (2018) report the discovery of [Fe XXI] in emission in a filament projected 1.9 kpc from the nucleus of M87. Theoretically, the highly ionized iron UV lines can be observed in absorption as well. The forbidden line of [Fe XXI], in particular, has the largest effective cross-section for absorption and a rest wavelength λ1354 Å, conveniently close to Ly α λ1215 Å.

In this work, we target the [Fe XXI] line in absorption as a tracer of high-redshift 10^7 K WHIM gas. Large optical spectroscopic quasar surveys available nowadays offer a new opportunity to statistically probe these filaments by detecting the matter between the high-redshift background quasar and the observer. Here, we make use of a large sample of high-spectral resolution quasar spectra with known intervening neutral gas damped Ly α absorbers (DLAs). Recent studies (Péroux et al. 2019; Hamanowicz et al. 2020) provide evidence for the paradigm of the origin of DLAs, showing that these objects probe overdensities (e.g. groups) in the Universe. We use these systems as tracers of foreground overdensities, and to increase the sensitivity of the experiment we stack multiple quasar spectra at the DLA's redshifts (Mas-Ribas et al. 2017) to look for indications of $T = 10^7$ K WHIM gas traced by the [Fe XXI] absorption line.

This manuscript is organized as follows: Section 2 presents the observations used for this study. Section 3 details the stacking method, while Section 4 summarizes our findings and future prospects with upcoming facilities. Throughout this paper, we adopt an $H_0 = 70$ km s^{-1} Mpc^{-1}, $\Omega_{\rm M} = 0.3$, and $\Omega_\Lambda = 0.7$ cosmology.

Downloaded from https://academic.oup.com/mnras/article/499/4/5230/5912396 by guest on 25 May 2024

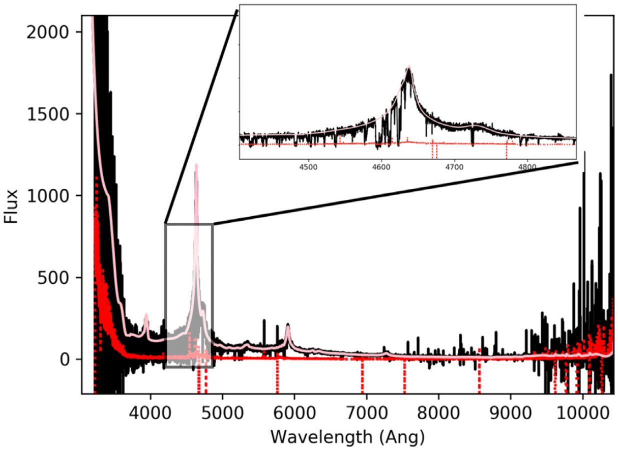

Figure 1. Example VLT/UVES quasar spectrum. The black histogram shows the full quasar spectrum at observed wavelengths and with arbitrary flux units. The quasar J000149−015939 at $z_{\rm em} = 2.815$ has a strong Ly α emission line at ∼4650 Å at rest frame. The red histogram displays the corresponding error array. The pink line indicates the fitted quasar continuum. The inset zooms around the Lyman α emission revealing the high snr$_{\rm ind}$.

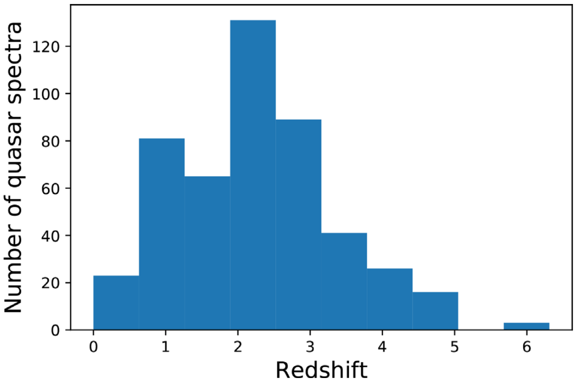

Figure 2. Quasar emission redshift distribution. The 467 UVES quasar spectra from the SQUAD sample cover a broad redshift range from $z_{\rm em}$ = 0 to 6, with wavelength coverage from 3050 to 10 500 Å with gaps depending on the chosen spectral settings.

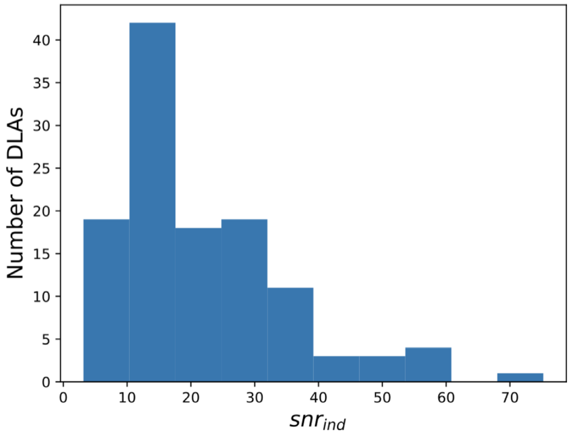

Figure 3. Signal-to-noise per resolution element (snr$_{\rm ind}$) distribution. The histogram shows the 155 UVES quasar spectra containing at least one DLA. The mean resolving power of the UVES spectrograph (R > 40 000) combined with an averaged exposure time of 5.9 h result in sizeable snr$_{\rm ind}$, reaching up to snr$_{\rm ind}$ > 70.

2 A LARGE SAMPLE OF HIGH-RESOLUTION QUASAR SPECTRA

To enhance the sensitivity to absorption line detection, this study focuses on the quasar spectra with the highest spectral resolution available. This work is based on a quasar sample observed with the Ultraviolet and Visual Echelle Spectrograph (UVES) of the European Southern Observatory's (ESO's) 8-metre Very Large Telescope (VLT) (Dekker et al. 2000). The UVES instrument is a two-arm (red and blue) grating cross-dispersed Echelle spectrograph. Some observations are made using only one arm, but most observations are done using both arms simultaneously. The light is then split in two by a dichroic mirror and centred around to a standard or user-defined central wavelength.

Our study makes use of the first release of the 'Spectral Quasar Absorption Database' (SQUAD) with 467 fully reduced, continuum-fitted quasar spectra (Murphy et al. 2019). Fig. 1 shows an example of a VLT/UVES quasar spectrum, with a zoom on the Lyman α quasar emission line. In this sample, the spectra were cross-matched with observations from the ESO UVES archives to include all quasars from literature up to 2017 August (Flesch 2015). The redshift was also cross-matched with three databases (SDSS, NED, and SIMBAD). In cases where no matches were found, a measure of the redshift was derived directly from the UVES spectrum. Fig. 2 illustrates the quasar redshift distribution of the whole sample. The redshifts range from $z_{\rm em} = 0$ to 6, with a broad wavelength coverage range (3050–10 500 Å) with gaps depending on the chosen spectral settings. The mean resolving power of the exposures is $R = 49\,000$. The corresponding resolution element is 6.1 km s^{-1}. The quasar spectra have on average a total exposure time of 5.9 h, resulting on sizeable signal-to-noise ratios per resolution element (hereafter snr$_{\rm ind}$, for individual quasar spectra), reaching up to snr$_{\rm ind}$ > 70. In other words, the full quasar sample is made of over 1450 h of VLT time observations. Fig. 3 displays the distribution of the snr$_{\rm ind}$ of the UVES quasar spectra.

Additionally, Murphy et al. (2019) provide a catalogue of 155 identified DLAs, out of which 18 are reported for the first time. The newly identified DLAs were found by visually checking the UVES quasar spectra. These DLAs are a class of quasar absorbers tracing high H I column density cold ($T = 10^4$ K) gas, with N(H I) ≥ 2×10^{20} (Wolfe et al. 1986). These systems comprise the majority of the neutral gas reservoir in the Universe used for the initial phase of star formation (e.g. Peroux & Howk 2020). Additionally, their metal content provides crucial information about the chemical evolution of galaxies. Fig. 4 displays the redshift distribution of this sample of 155 DLAs. Orange (green/red) histograms indicate the redshift of 2nd (3rd/4th) DLA in those quasar spectra containing more than one. The mean DLA redshift for the sample is $z_{\rm DLA} = 2.5$.

3 A STACKED HIGH-RESOLUTION DLA SPECTRUM

At the high-resolution (R > 40 000) offered by UVES, the metallicity of individual DLAs is routinely well measured (e.g. Kulkarni et al. 2005; De Cia et al. 2018; Poudel et al. 2020). In this work, we target weak metal lines that are not expected to be detected in a single spectra. In particular [Fe XXI] has an oscillator strength $f_{\rm osc} = 5.3 \times 10^{-6}$ and a Doppler parameter $b_{\rm Fe} = (2kT/m_{\rm Fe})^{1/2} \approx (54.4\,{\rm km\,s^{-1}})\,(T_7)^{1/2}$, where T_7 indicates at $T = 10^7$ K. In order to probe these significantly weaker absorption lines, we build a stack

Downloaded from https://academic.oup.com/mnras/article/499/4/5230/5912396 by guest on 25 May 2024

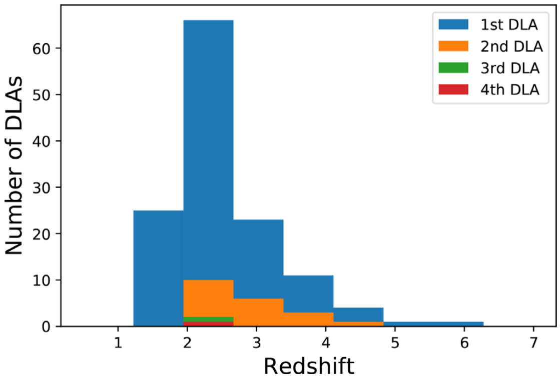

Figure 4. Redshift distribution of the 155 DLAs. Orange (green/red) histograms indicate the redshift of 2nd (3rd/4th) DLA in one given quasar spectrum. The mean DLA redshift for the sample is $z_{\mathrm{DLA}} = 2.5$.

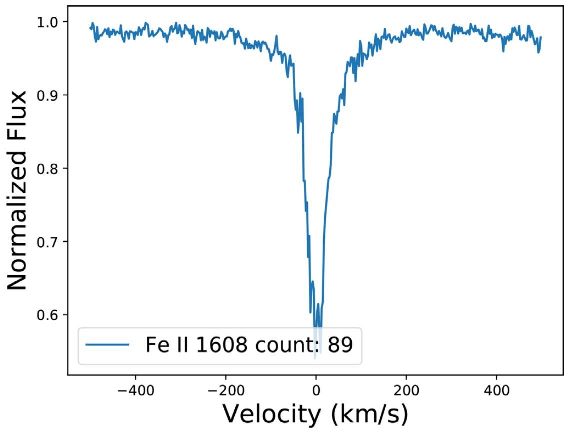

Figure 5. Example stack of a strong iron line. Stacking of 89 (as indicated in the legend) normalized UVES quasar spectra at the DLA position displays the detection of the Fe II $\lambda_{\mathrm{rest}}1608$ line.

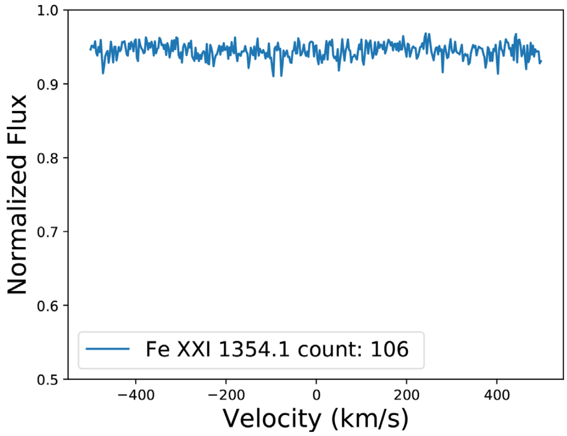

Figure 6. Stack of the weak [Fe XXI] line. Stacking of 106 (as indicated in the legend) normalized UVES quasar spectra at the DLA position lead to a non-detection of Fe XXI 1354 Å. The *y*-axis values are set to match those of Fig. 5.

of more than hundred high-resolution quasar spectra, shifted at the DLA redshifts.

3.1 Selecting quasar spectra

First, targeting DLAs to search for metal lines limits the number of quasar spectra to be stacked to the ones containing known DLAs. This step results in a sample of 155 quasar spectra out of the 467 contained in the whole SQUAD quasar sample.

Secondly, the dispersion of the UVES spectra, expressed in $\mathrm{km\,s^{-1}}$ per pixel, differs between five different values ranging from 1.3 $\mathrm{km\,s^{-1}}$ per pixel to 2.5 $\mathrm{km\,s^{-1}}$ per pixel. In order to prevent rebinning of the spectra during the stacking procedure, we elect to only include spectra with identical dispersion. A total of 137 spectra have a dispersion of 2.5 $\mathrm{km\,s^{-1}}$ per pixel which are then used in the subsequent study.

Finally, the spectral gaps in between the settings are evidenced by a visual inspection of the spectra. This gaps appear as flat lines in the middle of different parts of the spectra, where there is no signal. Only spectra with the appropriate wavelength coverage were included in further calculations depending on the location of the spectral gaps with respect to the targeted element at a given absorption redshift. This again caused a reduction of the number of spectra stacked depending on the element under study and its corresponding observed wavelength, where the count of the number of UVES spectra included for each element is stated on every plot. For each metal line stacked, we compute the number of spectra covering the appropriate wavelength given the DLA's redshift and the quasar spectrum wavelength coverage (in the rest frame ranging typically from λ1200 to 2600 Å). The number of spectra included in the stack of each metal line are therefore different. For example, [Fe XXI] has a final number of stacked spectra of 106.

Note that some quasars contain multiple DLAs at different redshifts (with cases containing up to four DLAs in one quasar spectrum), so some quasar spectra are used multiple times.

3.2 Stacking procedure

We first shift the selected spectra to the DLAs rest-frame wavelength. We recall that all spectra have the same dispersion of 2.5 $\mathrm{km\,s^{-1}}$ per pixel, so that no rebinning is required in building the stack in velocity space. We then use the resulting quasar spectra sample to compute a median stack. We reject spectra that do not fully cover the wavelength range ±500 $\mathrm{km\,s^{-1}}$ from the targeted metal feature. The corresponding number of quasar UVES spectra utilized are given in the legend of each of Figs 5, 6, and A1. At each pixel, we calculate the middle value of the ordered array of normalized fluxes from each quasar spectra. We also perform mean and weighted-mean stacks. Our results indicate that the median stack recovers the normalized quasar continuum better, with a higher resulting $\mathrm{SNR_{stack}}$ (for signal-to-noise of stack spectra) and less prominent contamination from interlopers. The median stack therefore provides the most stringent limits and is used in the subsequent analysis.

3.3 Strong metal line detections

The neutral gas probed by DLAs contains a wide variety of metals with different ionization states. These are tracing gas temperature of the order 10^4 K (Tumlinson et al. 2017). The metallicity of the DLAs evolves from $Z = 0.003\,\mathrm{Z_\odot}$ solar at redshift $z = 4$, to $Z = 0.15\,\mathrm{Z_\odot}$ solar at redshift $z = 1$ (Rafelski et al. 2012; De Cia et al. 2018;

Downloaded from https://academic.oup.com/mnras/article/499/4/5230/5912396 by guest on 25 May 2024

Peroux & Howk 2020; Poudel et al. 2020), with no DLAs found with a metallicity below 0.0025 solar (Meiksin 2009; Cooke & Fumagalli 2018).

The median stack spectrum results in the detection of several strong metal absorption lines commonly reported in DLAs which demonstrates the sensitivity of our approach. Fig. 5 shows an example of the median stack of 89 DLA spectra. The strong iron absorption line, Fe II ($\lambda_{\rm rest} = 1608$), is undoubtedly detected. The following 15 lines were detected at the redshift of the DLAs with a wavelength interval between 1200 an d 200 Å: iron (Fe II 1608 Å, Fe II 2600 Å), silicon (Si II 1260 Å, Si IV 1393 Å, Si IV 1403 Å), carbon (C IV 1548 Å, C IV 1551 Å), sulphur (S II 1259 Å), zinc (Zn II 2026 Å), oxygen (O I 1302 Å), chromium (Cr II 2026 Å), manganese (Mn II 2577 Å), nickel (Ni II 1317 Å), aluminium (Al II 1671 Å, Al III 1863 Å). These detections are reported in Fig. A1 of Appendix A.

4 PROBING THE WARM-HOT INTERGALACTIC MEDIUM

4.1 Observed [Fe XXI] column density limit

To search for tracers of the WHIM at UV wavelengths, we also stack forbidden UV lines of highly ionized iron which trace $T = 10^7$ K gas. The strongest of these line is [Fe XXI] at rest wavelength $\lambda1354.1$ (Anderson & Sunyaev 2016). This line is not detected in the stack spectrum as illustrated in Fig. 6. Another 15 weak metal lines were searched for but not detected. These include absorption lines like chlorine, argon, titanium, chromium, cobalt, germanium, arsenic, and krypton (Prochaska et al. 2003; Ellison et al. 2010).

To compute the equivalent width (EW) upper limit for this non-detection, we use the following relation (Ménard & Péroux 2003):

$$\mathrm{EW_{obs}} < \left[\frac{\sigma \times \mathrm{FWHM}}{\mathrm{SNR_{stack}}}\right]$$
$$\approx (77\,\mathrm{m\AA})\left(\frac{\sigma}{5}\right)\left(\frac{\mathrm{FWHM}}{1.43}\right)^{-1}\left(\frac{\mathrm{SNR_{stack}}}{93}\right)^{-1}, \qquad (1)$$

where we assume a σ value equal to 5, and compute the signal-to-noise ratio ($\mathrm{SNR_{stack}} = 93$) of the stacked spectrum in the velocity range $-500\ \mathrm{km\,s^{-1}} < v < 500\ \mathrm{km\,s^{-1}}$. The expected [Fe XXI] line is broad at the observed wavelength 4739 Å (1354.1 Å at a mean redshift of $\langle z\rangle = 2.5$). At $T = 10^7$ K, the Doppler parameter $b = 54.4\ \mathrm{km\,s^{-1}}$ and the FWHM $= 2(\ln 2)^{1/2}b = 90.6\ \mathrm{km\,s^{-1}}$ for a Gaussian line profile (Danforth et al. 2010; Keeney et al. 2012). We therefore assume a FWHM = 1.43 Å in equation (1). We compute the minimum observed equivalent width ($\mathrm{EW_{obs}} < 77$ mÅ) and convert it to rest-frame equivalent width $\mathrm{EW_{rest}} < 22$ mÅ. We compute the column density according to the linear relation between the equivalent width and the column density:

$$\mathrm{EW_{rest}} = \left(\frac{\pi e^2}{m_e c}\right)\frac{N f_{\rm osc}\lambda_{\rm rest}^2}{c} \approx (0.860\ \mathrm{m\AA})\left[\frac{N([\mathrm{Fe\,XXI}])}{10^{16}\ \mathrm{cm^{-2}}}\right], \qquad (2)$$

where c is the speed of light, m_e the electron mass, $\lambda_{\rm rest}$ is the rest wavelength of [Fe XXI], $\lambda_{\rm rest} = 1354$ Å, and $f_{\rm osc} = 5.3 \times 10^{-6}$ is the oscillator strength for [Fe XXI].

Reverting the equation, we compute the corresponding column density log[N([Fe XXI])] using the value of $\mathrm{EW_{rest}}$ ($\mathrm{EW_{rest}} < 22$ mÅ) as follows:

$$N([\mathrm{Fe\,XXI}]) = (10^{16}\ \mathrm{cm^{-2}})(\mathrm{EW_{rest}}/0.860\ \mathrm{m\AA}). \qquad (3)$$

The resulting column density limit in the stack of 106 DLAs observed in UVES quasar spectra at a mean redshift of $z_{\rm DLA} = 2.5$ is log[N([Fe XXI])] < 17.4, where all column densities are expressed in units of $\mathrm{cm^{-2}}$.

4.2 Expected [Fe XXI] column density

In order to put these results in context, we make two estimates of the expected column density of [Fe XXI] in gas typical of the WHIM and its corresponding EW. In both cases, we assume that [Fe XXI] corresponds to 20 per cent of the total iron abundance in the gas, i.e. an ionization fraction of $(\mathrm{Fe^{+20}/Fe}) = 0.2$. This hypothesis is born from modelling of gas in collisional ionization equilibrium (CIE) using the CHIANTI data base (Anderson & Sunyaev 2016). Then, we first assume the metallicity of the gas to be $Z_{\rm Fe} = 0.1\ Z_\odot$, i.e. $(Z_{\rm Fe}/Z_\odot) = 10^{-1}$. Given a specific element, F-e, we refer to the usual relation (e.g. Peroux & Howk 2020):

$$\mathrm{N_{FeXXI}} = \mathrm{N_{HI}}\left(\frac{\mathrm{Fe}}{\mathrm{H}}\right)_\odot\left(\frac{\mathrm{Fe^{+20}}}{\mathrm{Fe}}\right)\left(\frac{Z_{\rm Fe}}{Z_\odot}\right) = 3.55 \times 10^{14}\ \mathrm{cm^{-2}} \qquad (4)$$

where N(Fe) indicates the column density of the element Fe (surface density in atoms $\mathrm{cm^{-2}}$), $(Z_{\rm Fe}/Z_\odot)$ is the logarithmic abundance relative to the assumed solar abundance, and $\mathrm{N(Fe)/N(H)_\odot}$ is the reference solar abundance of both the element and hydrogen in the Solar System. Here, we adopt values of the Solar System abundances of Asplund et al. (2009) resulting in a column density of iron $\log[\mathrm{N(Fe)}]_\odot = 7.5$ and column density of hydrogen $\log[\mathrm{N(H)}]_\odot = 12$, meaning that $\log(\mathrm{Fe/H})_\odot = -4.50$.

Using the mean hydrogen column density of the DLAs in the sample: log[N(H I)] = 20.75, we calculate by assuming $(Z_{\rm Fe}/Z_\odot) = 10^{-1}$ that the WHIM gas will have an expected column density of log[N([Fe XXI])] ∼ 14.5. In a second hypothesis, we assume that the metallicity of the WHIM gas is $(Z_{\rm Fe}/Z_\odot) = 10^{-2}$, which then leads to an expected column density of log[N([Fe XXI])] ∼ 13.5. These column densities are about three orders of magnitude smaller than the upper limit derived from the stack of 106 UVES quasar spectra: log[N([Fe XXI])] < 17.4.

We note that in collisional ionization equilibrium (Shull & van Steenberg 1982), the ion fraction $f_{[\mathrm{Fe\,XXI}]} = (\mathrm{Fe^{+20}/Fe}) \sim 0.246$ peaks at $\log T = 7.0$, but falls off rapidly at lower temperatures: $f_{[\mathrm{Fe\,XXI}]} = 0.148$ ($\log T = 6.90$) and $f_{[\mathrm{Fe\,XXI}]} = 0.026$ ($\log T = 6.80$). Similar fall-off occurs at higher temperatures. Thus, the observed limits on N([Fe XXI]) are for a narrow temperature range, $\log T = 7.0 \pm 0.1$. The failure to detect [Fe XXI] could mean that the WHIM associated with the DLAs is cooler than $T = 10^{6.8}$ K. We note however that several recent studies have shown that DLA systems are primarily found in foreground overdensities (e.g. groups), which likely contains $\log T = 7.0$ gas (Péroux et al. 2019; Hamanowicz et al. 2020). Alternatively, to be able to detect such [Fe XXI] column density, one would need to significantly increase the number of spectra in order to get a higher $\mathrm{SNR_{stack}}$.

4.3 Future prospects of probing the WHIM at UV wavelengths

We now assess if this experiment with upcoming or planned facilities would enable to reach the [Fe XXI] column density to trace expected from the WHIM. First, we use equation (2) to compute the rest equivalent width corresponding to log[N([Fe XXI])] ∼ 14.5. We derive $\mathrm{EW_{rest}} = 0.03$ mÅ. Assuming a mean DLA redshift for the sample $z_{\rm DLA} = 2.5$, we compute a corresponding observed equivalent width of typically $\mathrm{EW_{obs}} = 0.1$ mÅ.

We look in turn into three type of facilities with high-resolution spectroscopic capabilities. First, we focus on the Multi-Object Spectrograph Telescope (4MOST), a high-multiplex spectroscopic

Downloaded from https://academic.oup.com/mnras/article/499/4/5230/5912396 by guest on 25 May 2024

survey instrument currently under construction phase for the 4m VISTA telescope of the European Southern Observatory (ESO). 4MOST is expected to start its science operations in 2023. It has a wide field of view of 2.5 deg diameter and nearly 2400 fibres dividing in two different types of spectrographs. We here focus on the high-resolution fibres, offering nearly 800 spectra with a spectral resolution $R \sim 20\,000$ (FWHM = 0.2 Å at 6000 Å) over a wavelength coverage λ3920 to 6750 (Quirrenbach & 4MOST Consortium 2015). For a typical exposure time of 2 h, 4MOST will deliver quasar spectra with an average $\mathrm{snr_{ind}} = 10$ for a mag <19 object (de Jong et al. 2019). We note that the WEAVE instrument designed for the William Herschel Telescope (WHT) will offer comparable characteristics in the Northern hemisphere (Pieri et al. 2016).

Secondly, we consider the high-resolution spectrograph (HIRES) for the 39m Extremely Large Telescope (ELT) currently under construction. HIRES (Marconi et al. 2018), which has successfully completed its Phase A, has a large spectral coverage ranging from 4000 to 25 000 Å with a spectral resolution $R = 100\,000$ (FWHM = 0.04 Å at 6000 Å). HIRES is not a survey instrument, as opposed to the other facilities described here, being both a single-target spectrograph and a facility open to the community for small and medium-size proposals. However, the ESO open-archives policy (Romaniello et al. 2018) means that significant number of quasar spectra will become publicly available after few years of operations. Depending on the science goals, we expect quasar spectra to be recorded with $\mathrm{snr_{ind}}$ varying from 10 to 1000. Here, we assume a medium $\mathrm{snr_{ind}}$ per spectra of $\mathrm{snr_{ind}} = 50$.

Finally, we look further out in the future for upcoming facilities for multi-object spectrographs on 10m class telescopes. The Maunakea Spectroscopy Explorer (MSE) is being proposed to replace the Canada–France–Hawaii Telescope (CFHT) (The MSE Science Team 2019). With 1.52 $\mathrm{deg^2}$ field of view, it will have the capability of simultaneously observe more than 4000 objects. At low spectral resolution ($R \sim 3650$), an $\mathrm{snr_{ind}}$ of 2 for magnitude 24 sources will be achieved in 1 h observation. At high spectral resolution ($R \sim 40\,000$; FWHM = 0.1 Å at 6000 Å), a $\mathrm{snr_{ind}} = 20$ for magnitude 20 source will be obtained typically in a little over 1-h exposure. A conceptual design study for an analogous facility in the Southern hemisphere has also been put forward. The so-called Spectroscopic Survey Telescope, here after SpecTel (Ellis et al. 2017), will offer a field of view of 5 $\mathrm{deg^2}$ and will be equipped with 15 000 fibres covering a wavelength range of 3600 Å $< \lambda <$ 13 300 Å.

The characteristics of each of these facilities are summarized in the first three lines of Table 1. We next estimate the $\mathrm{SNR_{stack}}$ of the stack quasar spectrum required to reach the expected observed equivalent width of $\mathrm{EW_{obs}} = 0.1$ mÅ to detect a $\log[N([\mathrm{Fe\,XXI}])] \sim 14.5$ absorption feature at $\sigma = 3$. To this end, we revert equation 1 and derive $\mathrm{SNR_{stack}} = 42\,900$. We note that given the width of the [Fe XXI] line (FWHM = 1.43 Å), this calculation is independent of the spectral resolution of the instrument. We then compute the number of spectra, N, needed for each facility to reach the necessary $\mathrm{SNR_{stack}}$ in the stack spectrum that will allow one to detect [Fe XXI] in WHIM gas:

$$N > \left[\frac{\mathrm{SNR_{stack}}}{\mathrm{snr_{ind}}}\right]^2. \quad (5)$$

We find that 4MOST, ELT/HIRES, and MSE/SpecTel will require respectively >18M, >700k, and >4M quasar spectra to achieve the required sensitivity. The high-multiplexing capabilities of 4MOST, MSE, and SpecTel mean that large samples can be acquired in a few years, although these large number of spectra are unrealistic at present. The experiment we explore here would benefit from cumulating data from existing and upcoming quasar surveys (e.g. Liske et al. 2008; Merloni et al. 2019).

Table 1. Number spectra needed for each facility to reach the $\mathrm{SNR_{stack}}$ necessary to detect [Fe XXI] in the WHIM at $\sigma = 3$. The first two rows indicate the spectral resolution of the facilities expressed as R and in Å as FWHM at 6000 Å. The third row provides the required $\mathrm{SNR_{stack}}$ of the stack spectra to reach the $\mathrm{EW_{obs}} = 0.1$ mÅ required to detect [Fe XXI]. The fourth row states the mean $\mathrm{snr_{ind}}$ of individual spectra foreseen for these facilities given a typical exposure time. Finally, the last row provides the number of quasar spectra required to achieve the corresponding $\mathrm{SNR_{stack}}$ in the stack spectra. Note that while the unmatched high spectral resolution of ELT/HIRES leads to a smaller number of spectra, this facility does not provide the multiplexing capabilities of other telescopes (4MOST, MSE/SpecTel).

Facilities	4MOST	ELT/HIRES	MSE/SpecTel
Spectral resolution, R	20 000	100 000	40 000
FWHM (Å)	0.2	0.04	0.1
Required $\mathrm{SNR_{stack}}$ to reach $\mathrm{Ew_{obs}} = 0.1$ mÅ	42 900	42 900	42 900
Individual $\mathrm{snr_{ind}}$	10	50	20
Number of spectra	>18M	>700k	>4M

To put these results in context, we stress that this experiment is complementary to approaches planned at X-ray wavelengths with upcoming facilities. In coming decades, next-generation spacecrafts will aim at solving fully the missing baryons problem. The ESA *Athena* mission with spectroscopic and imaging capabilities in the 0.5–12 keV range will significantly further our understanding of the baryons in the Universe, both inside the potential wells of groups and clusters of galaxies and in the WHIM in filaments between the densest regions in the Cosmos (Barret et al. 2020). Investigating how such potential wells formed and evolved, and how and when the material trapped in them was energized and chemically enriched, can uniquely be tackled by observations in the X-ray band, combining wide-field images with high-resolution spectroscopy, both of high sensitivity. Similarly, *Lynx*, a mission proposed to NASA in the framework of the next flagship space telescope, will have total effective area greater than 2 $\mathrm{m^2}$ at 1 keV (Falcone et al. 2019). These facilities will provide a new window in our capability to characterize the physical processes of the WHIM. However, these exposures will reveal single WHIM detections, while the detection of [Fe XXI] in stack quasar spectra will offer a complementary way to characterize the physical properties of the WHIM in a statistical manner. By reverting to a statistical approach, this technique is less prone to uncertainties related to variation from object to object in the Universe (the so-called cosmic variance).

5 CONCLUSION

In this work, we target the [Fe XXI] line in absorption as a tracer of high-redshift 10^7 K WHIM gas. We make use of a large sample of high-spectral resolution quasar spectra with known intervening neutral gas damped Ly α absorbers (DLAs). To enhance the sensitivity to absorption line detection, this study focuses on high spectral resolution ($R \sim 49\,000$) quasar spectra from VLT/UVES. To increase the sensitivity of the experiment, we stack 106 quasar spectra at DLA's redshifts to look for indications of 10^7 K WHIM gas traced by the [Fe XXI] absorption line. We report a limit on the column density in the stack of $\log[N([\mathrm{Fe\,XXI}])] < 17.4\mathrm{cm^{-2}}$. Using basic assumptions on properties of 10^7 K gas, we calculate that the WHIM will result in an expected column density of the order $\log[N([\mathrm{Fe\,XXI}])] \sim 14.5\mathrm{cm^{-2}}$, almost three orders of magnitude

Downloaded from https://academic.oup.com/mnras/article/499/4/5230/5912396 by guest on 25 May 2024

smaller than the derived upper limit. We then analyse the capabilities of future facilities, namely 4MOST, ELT/HIRES, and MSE/SpecTel to detect such gas. We compute the number of spectra that would be needed from each facilities to reach the signal-to-noise ratio required for the detection of [Fe XXI] absorption line in 10^7 K WHIM gas. We find that 18M high-resolution fibre 4MOST, 700k ELT/HIRES, or 4M MSE/TechSpec quasar spectra are required. We have explored here an alternative method that this experiment could be initiated by cumulating samples from existing and planned quasar surveys with these facilities. In conclusion, we study here an alternative to X-ray detected WHIM tracers. While a significantly weaker line, redshifted [Fe XXI] 1354 Å is observable at optical wavelengths from the ground, benefiting from higher instrumental throughput, enhanced spectral resolution, longer exposure times, and increased number of targets.

ACKNOWLEDGEMENTS

We thank Michael Murphy and collaborators for making reduced and combined UVES quasar spectra publicly available to the community. We are grateful to the referee, Mike Shull, for a thorough report.

DATA AVAILABILITY

The data underlying this article are available in [UVES_SQUAD_DR1], at [doi:10.1093/mnras/sty2834]. The data sets were derived from sources in the public domain: [https://github.com/MTMurphy77/UVES_SQUAD_DR1;].

REFERENCES

Aghanim N. et al., 2016, A&A, 607
Anderson M. E., Sunyaev R., 2016, MNRAS, 459, 2806
Anderson M. E., Sunyaev R., 2018, A&A, 617, A123
Arcodia R., Campana S., Salvaterra R., Ghisellini G., 2018, A&A, 616, A170
Asplund M., Grevesse N., Sauval A. J., Scott P., 2009, ARA&A, 47, 481
Augustin R. et al., 2019, MNRAS, 489, 2417
Barcons X. et al., 2011, preprint (arXiv:1207.2745)
Barret D., Decourchelle A., Fabian A., Guainazzi M., Nandra K., Smith R., den Herder J.-W., 2020, Astron. Nachr., 341, 224
Bertone S., Schaye J., Dolag K., 2008, Space Sci. Rev., 134, 295
Bonamente M., Nevalainen J., Tilton E., Liivamägi J., Tempel E., Heinämäki P., Fang T., 2016, MNRAS, 457, 4236
Bregman J. N., 2007, ARA&A, 45, 221
Cen R., Ostriker J. P., 1999, ApJ, 514, 1
Cooke R. J., Fumagalli M., 2018, Nat. Astron., 2, 957
Danforth C. W., Shull J. M., 2005, ApJ, 624, 555
Danforth C. W., Shull J. M., 2008, ApJ, 679, 194
Danforth C. W., Stocke J. T., Shull J. M., 2010, ApJ, 710, 613
Danforth C. W. et al., 2016, ApJ, 817, 111
Davé R. et al., 2001, ApJ, 552, 473
De Cia A., Ledoux C., Petitjean P., Savaglio S., 2018, A&A, 611, A76
de Graaff A., Cai Y.-C., Heymans C., Peacock J. A., 2019, A&A, 624, A48
de Jong R. S. et al., 2019, The Messenger, 175, 3
Dekker H., D'Odorico S., Kaufer A., Delabre B., Kotzlowski H., 2000, in Iye M., Moorwood A. F., eds, Proc. SPIE Conf. Ser. Vol. 4008, Optical and IR Telescope Instrumentation and Detectors. SPIE, Bellingham, p. 534
DeRoo C. T. et al., 2020, ApJ, 897, 92
Ellis R. S. et al., 2017, preprint (arXiv:1701.01976)
Ellison S. L., Prochaska J. X., Hennawi J., Lopez S., Usher C., Wolfe A. M., Russell D. M., Benn C. R., 2010, MNRAS, 406, 1435
Falcone A. D., Kraft R. P., Bautz M. W., Gaskin J. A., 2019, Proc. Conf., LPI Contribution No. 2135, The Space Astrophysics Landscape for the 2020s and Beyond. Potomac, Maryland, p. 5043
Flesch E. W., 2015, Publ. Astron. Soc. Aust., 32, e010
Frank S., Mathur S., Pieri M., York D. G., 2010, AJ, 140, 835
Galeazzi M., Gupta A., Huffenberger K., Ursino E., 2010, American Astronomical Society, AAS Meeting #216, id.318.04
Gupta A., Mathur S., Krongold Y., Nicastro F., Galeazzi M., 2012, ApJ, 756, L8
Hamanowicz A. et al., 2020, MNRAS, 492, 2347
Hill J. C., Ferraro S., Battaglia N., Liu J., Spergel D. N., 2016, Phys. Rev. Lett., 117, 051301
Ho S., Dedeo S., Spergel D., 2009, preprint (arXiv:0903.2845)
Howk J. C., Ribaudo J. S., Lehner N., Prochaska J. X., Chen H.-W., 2009, MNRAS, preprint (arXiv:0903.3963)
Johnson S. D. et al., 2019, ApJ, 884, L31
Keeney B. A., Danforth C. W., Stocke J. T., France K., Green J. C., 2012, PASP, 124, 830
Kim J.-G., Kim W.-T., 2013, ApJ, 779, 48
Kovács O. E., Bogdán Á., Smith R. a. K., Kraft R. P., Forman W. R., 2019, ApJ, 872, 83
Kulkarni V. P., Fall S. M., Lauroesch J. T., York D. G., Welty D. E., Khare P., Truran J. W., 2005, ApJ, 618, 68
Lehner N., Savage B. D., Richter P., Sembach K. R., Tripp T. M., Wakker B. P., 2007, ApJ, 658, 680
Li J.-T., 2020, Astron. Nachr., 341, 177
Lim S. H., Mo H. J., Wang H., Yang X., 2020, ApJ, 889, 48
Liske J. et al., 2008, MNRAS, 386, 1192
Macquart J. P. et al., 2020, Nature, 581, 391
Marconi A. et al., 2018, Proc. SPIE, 10702, 107021Y
Martizzi D. et al., 2019, MNRAS, 486, 3766
Mas-Ribas L. et al., 2017, ApJ, 846, 4
Mathur S., Nicastro F., Gupta A., Krongold Y., McLaughlin B. M., Brickhouse N., Pradhan A., 2017, ApJ, 851, L7
Meiksin A. A., 2009, Rev. Mod. Phys., 81, 1405
Ménard B., Péroux C., 2003, A&A, 410, 33
Merloni A. et al., 2019, The Messenger, 175, 42
Murphy M. T., Kacprzak G. G., Savorgnan G. A. D., Carswell R. F., 2019, MNRAS, 482, 3458
Narayanan A. et al., 2011, ApJ, 730, 15
Nevalainen J. et al., 2019, A&A, 621, A88
Nicastro F. et al., 2018, Nature, 558, 406
Pachat S., Narayanan A., Muzahid S., Khaire V., Srianand R., Wakker B. P., Savage B. D., 2016, MNRAS, 458, 733
Peroux C., Howk J. C., 2020, ARA&A, 58, 363
Péroux C. et al., 2019, MNRAS, 485, 1595
Persic M., Salucci P., 1992, MNRAS, 258, 14P
Pieri M. M. et al., 2016, in Reylé C., Richard J., Cambrésy L., Deleuil M., Pécontal E., Tresse L., Vauglin I., eds, SF2A-2016: Proceedings of the Annual meeting of the French Society of Astronomy and Astrophysics. Centre de Recherche Astrophysique de Lyon, p. 259
Poudel S., Kulkarni V. P., Cashman F. H., Frye B., Péroux C., Rahmani H., Quiret S., 2020, MNRAS, 491, 1008
Prochaska J. X., Gawiser E., Wolfe A. M., Castro S., Djorgovski S. G., 2003, ApJ, 595, L9
Prochaska J. X. et al., 2017, ApJ, 837, 169
Qiang D.-C., Wei H., 2020, J. Cosmol. Astropart. Phys., 2020, 023
Quirrenbach A., 4MOST Consortium, 2015, IAU General Assembly, Meeting #29, id.2258057
Rafelski M., Wolfe A. M., Prochaska J. X., Neeleman M., Mendez A. J., 2012, ApJ, 755, 89
Romaniello M. et al., 2018, The Messenger, 172, 2
Salucci P., Persic M., 1999, MNRAS, 309, 923
Sanchez S. F., Morisset C., Delgado-Inglada G., eds., 2016, Proc. Conf., The Interplay between Local and Global Processes in Galaxies. Cozumel, Mexico
Savage B. D., Kim T. S., Wakker B. P., Keeney B., Shull J. M., Stocke J. T., Green J. C., 2014, ApJS, 212, 8
Shull J. M., van Steenberg M., 1982, ApJS, 48, 95
Shull J. M., Smith B. D., Danforth C. W., 2012, ApJ, 759, 23
Tanimura H., Aghanim N., Bonjean V., Malavasi N., Douspis M., 2020, A&A, 637, A41

Downloaded from https://academic.oup.com/mnras/article/499/4/5230/5912396 by guest on 25 May 2024

The MSE Science Team, 2019, preprint (arXiv:1904.04907)
Tripp T. M., Savage B. D., Jenkins E. B., 2000, ApJ, 534, L1
Tripp T. M., Sembach K. R., Bowen D. V., Savage B. D., Jenkins E. B., Lehner N., Richter P., 2008, ApJS, 177, 39
Tumlinson J., Peeples M. S., Werk J. K., 2017, ARA&A, 55, 389
Wang Q. D., Yao Y., 2012, preprint (arXiv:1211.4834)
Werk J. K., Prochaska J. X., Thom C., Tumlinson J., Tripp T. M., O'Meara J. M., Peeples M. S., 2013, ApJS, 204, 17
Werk J. K. et al., 2014, ApJ, 792, 8
Wijers N. A., Schaye J., Oppenheimer B. D., 2020, MNRAS, 498, 574
Wolfe A. M., Turnshek D. A., Smith H. E., Cohen R. D., 1986, ApJS, 61, 249
Zastrocky T. E., Howk J. C., Lehner N., O'Meara J. M., 2018, Res. Notes Am. Astron. Soc., 2, 227

APPENDIX: STRONG METAL LINES DETECTIONS

The figure in this appendix reports the detection of multiple strong metal lines in UVES stacked quasar spectra at the DLA redshift.

Downloaded from https://academic.oup.com/mnras/article/499/4/5230/5912396 by guest on 25 May 2024

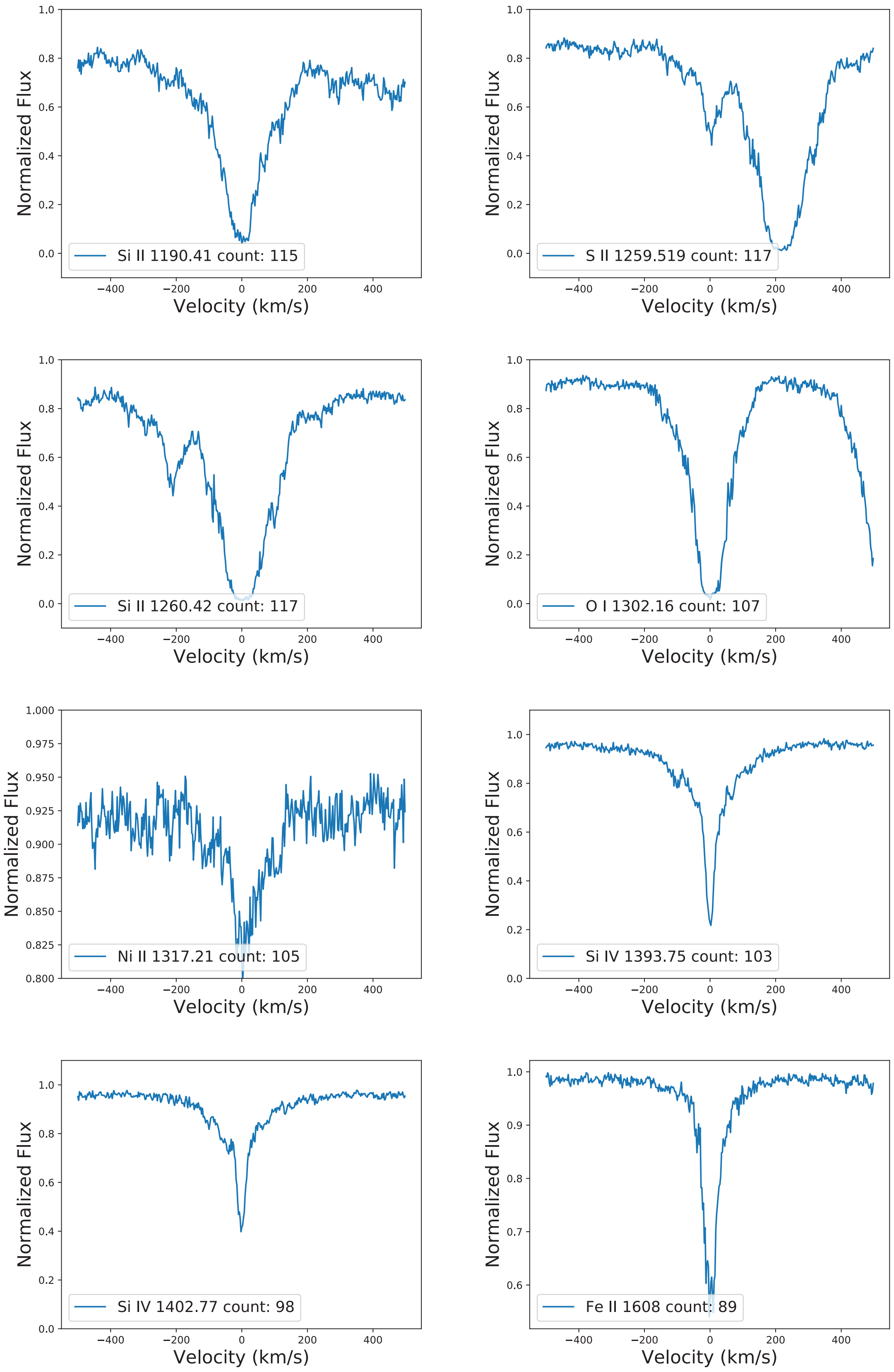

Figure A1. Stack of strong metal lines at the DLA redshift. The number of stacked normalized UVES quasar spectra are indicated in the legend for each element as well as the rest wavelength of the metal line. The mean redshift of the DLAs sample is $z_{\rm DLA} = 2.5$. The dropping continuum levels in the C IV panels indicate the presence of the other member of the doublet, while in O I panel it is due to nearby Si II 1304 Å absorption.

Downloaded from https://academic.oup.com/mnras/article/499/4/5230/5912396 by guest on 25 May 2024

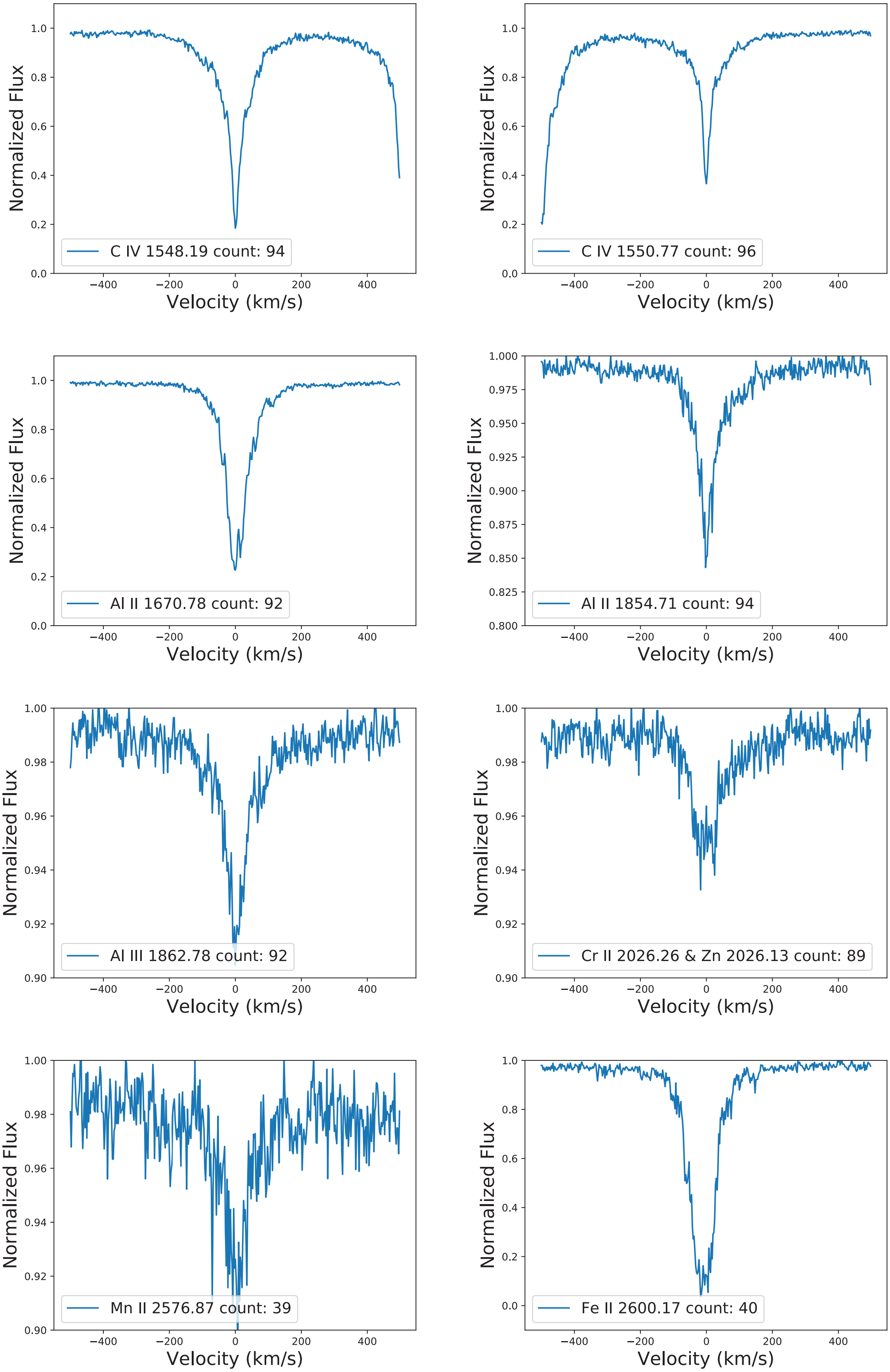

Figure A1 – *continued*

Downloaded from https://academic.oup.com/mnras/article/499/4/5230/5912396 by guest on 25 May 2024

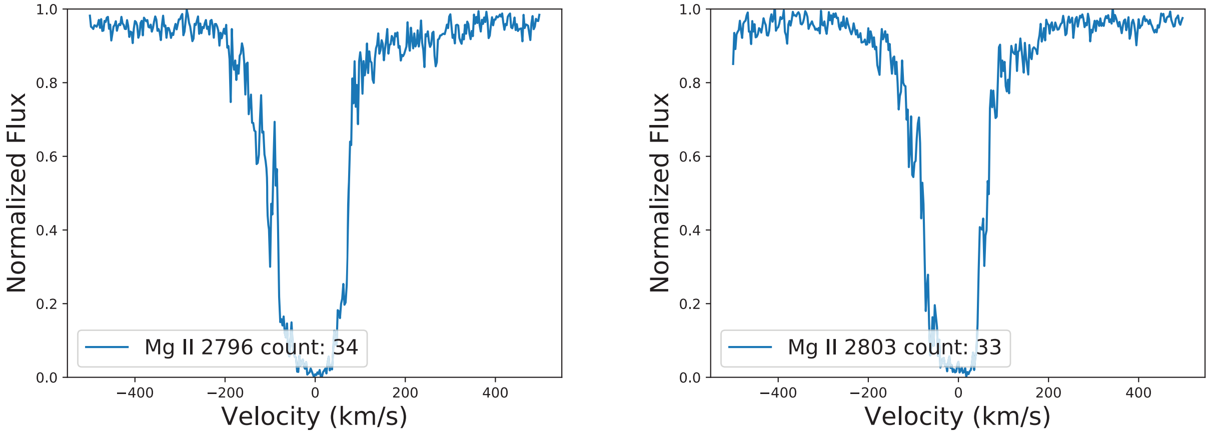

Figure A1 – *continued*

This paper has been typeset from a TEX/LATEX file prepared by the author.

Downloaded from https://academic.oup.com/mnras/article/499/4/5230/5912396 by guest on 25 May 2024